Supplemental Information

Flexural Rigidity and Shear Stiffness of Flagella Estimated from Induced Bends and Counterbends

Gang Xu, Kate S. Wilson, Ruth J. Okamoto, Jin-Yu Shao, Susan K. Dutcher, and Philip V. Bayly

Appendix A. Apparent flexural rigidity of beams with both flexural rigidity and shear stiffness

We compare the apparent flexural rigidity of a beam with shear stiffness, simply supported and loaded at the midpoint (three-point bending), to the apparent flexural rigidity of the fixed-free beam (Eq. 10 in the main text). The equilibrium equations for beam with intrinsic flexural rigidity EI and shear resistance k_s in three-point bending with central load F (**Fig. A1**) are.

$$EI \frac{\partial^2 \theta}{\partial s^2} - k_s \theta = -\frac{F}{2}. \qquad 0 < s < \frac{L}{2} \qquad (A.1a)$$

$$EI \frac{\partial^2 \theta}{\partial s^2} - k_s \theta = +\frac{F}{2}. \qquad \frac{L}{2} \leq s < L \qquad (A.1b)$$

Relevant boundary conditions for the beam are:

$$\left. \frac{\partial \theta}{\partial s} \right|_{s=0} = 0, \qquad \theta|_{s=L/2} = 0, \qquad (A.2)$$

The solution for the tangent angle of the beam in the left half of the beam is:

$$\theta(s) = \frac{F}{2k_s} \left(1 - \frac{e^{\beta s} + e^{-\beta s}}{e^{\beta L/2} + e^{-\beta L/2}} \right), \qquad 0 < s < \frac{L}{2}. \qquad (A.3)$$

where $\beta^2 = k_s/EI$.

The deflection at the midpoint in three-point bending in beam:

$$\delta = y(L/2) = \int_0^{L/2} \theta ds = \frac{FL}{4k_s} \left(1 - \frac{2}{\beta L} \cdot \frac{e^{\beta L/2} - e^{-\beta L/2}}{e^{\beta L/2} + e^{-\beta L/2}} \right). \qquad (A.4)$$

For comparison, the deflection at the midpoint of an ideal Euler-Bernouilli beam with no shear resistance, in three-point bending is: $\delta_0 = \frac{FL^3}{48EI}$. Accordingly we define the apparent flexural rigidity of a beam with shear resistance, in three-point bending as: $\overline{EI} = \frac{FL^3}{48\delta}$. The ratio of apparent flexural rigidity to intrinsic flexural rigidity is thus.

$$\frac{\overline{EI}}{EI} = \frac{\delta_0}{\delta} = \frac{\beta^3 L^3}{12 \left(\beta L - 2 \cdot \frac{e^{\beta L/2} - e^{-\beta L/2}}{e^{\beta L/2} + e^{-\beta L/2}} \right)} \qquad (A.5)$$

As expected, this ratio approaches unity in the limit as $\beta L \to 0$, and increases with βL.
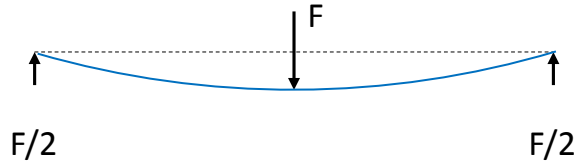

Figure A1. Free-body diagram of beam in three-point bending.

Comparing Eq. A.5 with Eq. 10 of this paper, we see that the apparent flexural rigidity of beams, for a given shear stiffness, increases with length in both loading scenarios, but at different rates. This can be seen in the graph of the non-dimensional ratio $\overline{EI}/EI$ vs the non-dimensional parameter βL (Fig. S2). The dimensional value of apparent flexural rigidity , $\overline{EI}$, is plotted vs length for representative parameter values, for both three-point bending of a simply-supported beam and tip loading of a fixed-free beam. It is clear that the two measurement protocols give very different estimates of $\overline{EI}$, and that the estimates diverge as length increases.
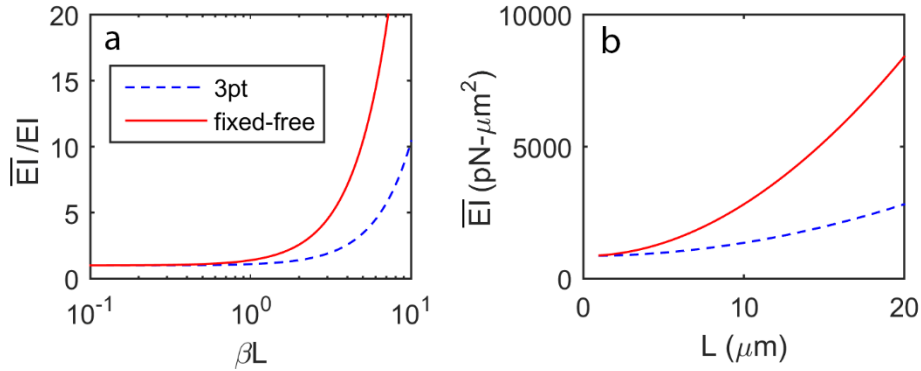

Figure A2. (a) Non-dimensional ratio of apparent flexural rigidity $\overline{EI}$ to intrinsic flexural rigidity EI for beams under different test conditions, as a function of the non-dimensional parameter βL. (b) Apparent (dimensional) flexural rigidity $\overline{EI}$ of a beam with intrinsic flexural rigidity $EI = 860 \text{ pN} \cdot \mu m^2$ and shear stiffness $k_s = 50 \text{ pN/rad}$, under different test conditions. Solid red curves: $\overline{EI}$ estimated from the deflection of a fix-free beam loaded at the tip. Dashed blue curves: $\overline{EI}$ estimated from the deflection at the mid-point of a simply-supported beam loaded at its midpoint (three-point bending).
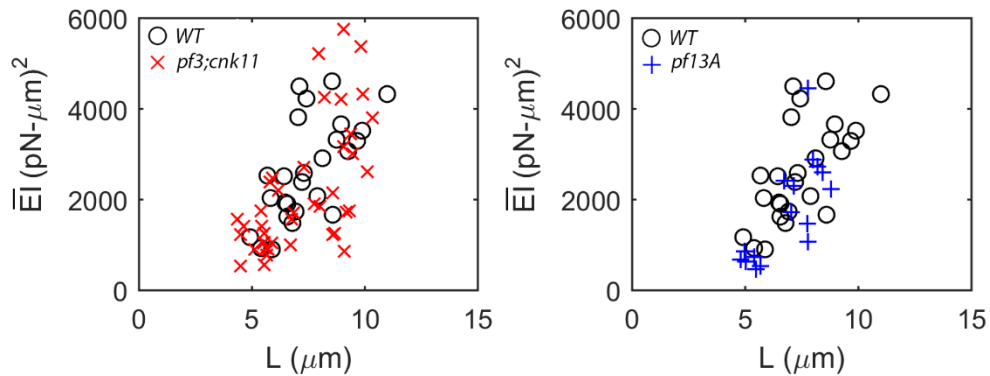

Figure A3. Apparent flexural rigidity $\overline{EI}$ of flagella measured by optical trap technique in wild-type *Chlamydomonas*, and in *pf3; cnk11-6* and *pf13A* mutants.

Appendix B. Details of the closed form solution for the counterbend experiment

The analytical solution for the shape of a beam subjected to a perpendicular point load at s_0 is given by Eqs. (12-16) from the main text:

$$\theta(s) = \theta_1(s) = \frac{F}{k_s} + c_1 e^{\beta s} + c_2 e^{-\beta s}, \qquad s < s_0, \qquad (12a)$$

$$\theta(s) = \theta_2(\gamma) = d_1 e^{\beta \gamma} + d_2 e^{-\beta \gamma}, \qquad s \geq s_0, \quad \gamma = s - s_0. \qquad (12b)$$

The four boundary conditions (Eqs. 13-16 in the paper) are also repeated here:

$$BC_1: \quad \theta_1|_{s=0} = 0, \qquad (13)$$

$$BC_2: \quad \left.\frac{\partial \theta}{\partial s}\right|_{s=L} = \left.\frac{\partial \theta_2}{\partial \gamma}\right|_{\gamma=\gamma_0} = 0, \quad (\gamma_0 = L - s_0) \qquad (14)$$

$$BC_3: \quad \theta_1|_{s=s_0} = \theta_2|_{\gamma=0}, \qquad (15)$$

$$BC_4: \quad \left.\frac{\partial \theta_1}{\partial s}\right|_{s=s_0} = \left.\frac{\partial \theta_2}{\partial \gamma}\right|_{\gamma=0} \qquad (16)$$

These boundary conditions lead to algebraic equations which determine the four coefficients (c_1, c_2, d_1, d_2) for given values of F, k_s (or EI), β, L, and s_0.

$$BC_1: \quad \frac{F}{k_s} + c_1 + c_2 = 0, \qquad (B.1)$$

$$BC_2: \quad \beta\left(d_1 e^{\beta \gamma_0} - d_2 e^{-\beta \gamma_0}\right) = 0, \qquad (B.2)$$

$$BC_3: \quad \frac{F}{k_s} + c_1 e^{\beta s_0} + c_2 e^{-\beta s_0} = d_1 + d_2, \qquad (B.3)$$

$$BC_4: \quad \beta\left(c_1 e^{\beta s_0} - c_2 e^{-\beta s_0}\right) = \beta(d_1 - d_2). \qquad (B.4)$$

where $\gamma_0 = L - s_0$ (the length of the section distal to the point load).

These equations may be solved simultaneously to give the coefficients

$$c_2 = \frac{F}{k_s} \frac{\left(\dfrac{1 - e^{-\beta s_0}}{e^{\beta s_0} - e^{-\beta s_0}} - \dfrac{e^{-\beta s_0}}{e^{\beta s_0} + e^{-\beta s_0}}\right)}{\left(\dfrac{1 + e^{2\beta \gamma_0}}{e^{\beta s_0} - e^{-\beta s_0}} - \dfrac{1 - e^{2\beta \gamma_0}}{e^{\beta s_0} + e^{-\beta s_0}}\right)} \qquad (B.5)$$

$$c_1 = c_2 \left(\frac{1 - e^{2\beta \gamma_0}}{e^{\beta s_0} + e^{-\beta s_0}}\right) - \frac{\left(\dfrac{F}{k_s}\right) e^{-\beta s_0}}{e^{\beta s_0} + e^{-\beta s_0}} \qquad (B.6)$$

$$d_1 = -c_1 - \frac{F}{k_s} \qquad (B.7)$$

$$d_2 = c_2 e^{2\beta \gamma_0} \qquad (B.8)$$

Appendix C. General relationships between tip compliance and flagellar length

If the tip deflection in response to a point load were solely due to simple bending (as in an Euler-Bernouilli beam with flexural rigidity EI) the tip compliance would be:

$$C = \frac{\delta}{F} = \frac{L^3}{3EI} \qquad (C.1)$$

If the tip deflection were solely due to rotation at the base, subject to the restoring force of a spring with torsional stiffness k_B (pN · μm/rad) the tip compliance would be:

$$C = \frac{\delta}{F} = \frac{L^2}{k_B} \qquad (C.2)$$

If the tip deflection were solely due to shear deformation, resisted by shear stiffness k_s (pN/rad) the tip compliance would be:

$$C = \frac{\delta}{F} = \frac{L}{k_s} \qquad (C.3)$$

For the first case (pure bending) the log-log plot of compliance vs. length would have a slope of 3, in the second case (pure base rotation) the log-log plot would have a slope of 2, and in the third case the log-log plot would have a slope of 1.

Figure C1 shows the raw compliance measurements for wild-type, *pf3; cnk11-6,* and *pf13A* mutants plotted on log-log scales. Also shown are simple linear fits to the log-log data.
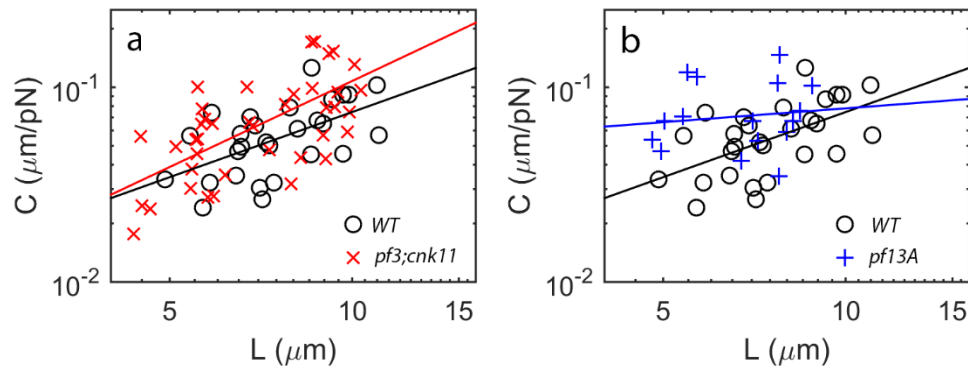

Figure C1. Log-log plots of tip compliance vs flagellar length in Chlamydomonas flagella, measured using optical tweezers. The slopes of the best-fit lines to the log-log data are 1.11 (wild-type), 1.47 (*pf3; cnk11-6*) and 0.24 (*pf13A*).

The slopes of the log-log plots of compliance vs length are all much less than 3. Since counterbend experiments confirm minimal rotation at the base, it is likely that shear stiffness plays an important role in determining the tip compliance. The very low slope of the compliance-length relationship in the *pf13A* mutant suggests unmodeled physical characteristics, such as a non-uniform longitudinal distribution of shear stiffness.

Appendix D. Structural finite element models of flagellar bending

To directly examine the effect of inter-doublet sliding resistance on the overall apparent flexural rigidity and the counterbend response of the axoneme, nonlinear 2D finite-element computational models for the axoneme were created, using the finite-element software ABAQUS (v.6.7, Abaqus, Inc., Providence, RI). Utilizing built-in mechanical elements in the software, the microtubule doublets were represented by two elastic beams (10 μm long and 240 nm separation) and all interconnecting structures (nexin links, radial spokes, e.g.) by an array of 100 trusses (to control spacing) and 100 springs (to resist sliding) (Fig. D1). Despite its simplicity, this axoneme model recapitulates the overall structural and mechanical properties of the axoneme. The intrinsic flexural rigidity (EI pN·μm2) was provided by two beam elements each with flexural rigidity $EI/2$, while the values of the elastic constant, k_k, for the springs were varied over a wide range.
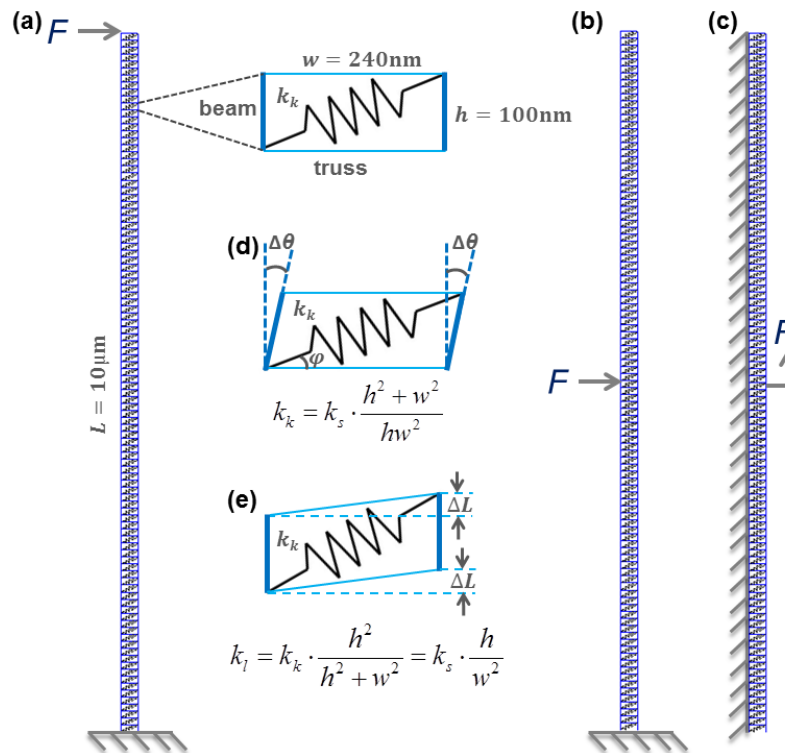

Figure D1. The 2D finite element model of the axoneme. The axoneme is modeled as two 10-μm-long elastic beams cross-linked by an array of 100 truss elements (to maintain spacing) and 100 springs (to resist sliding, inset in a). (a) A concentrated force is applied perpendicular to the beam at the tip of the beam, to cause a slight bending deformation (in analogy to the optical tweezers experiment). (b) A concentrated force is applied perpendicular to the beam at the mid-point to bend the proximal half of the beam (as in the counterbend experiment). Models in (a) and (b) were used to study how the apparent flexural rigidity and the counterbend response of the beam depend on the inter-beam shear stiffness provided by the interconnecting springs. (c) A concentrated force along the longitudinal axis of the beam is applied at the mid-point to cause a small shear displacement of one beam relative to the other, as in Minoura et al [1]. (d) For small deflections, the elasticity of the springs, k_k, is directly related to the shear stiffness, k_s, through Eq. D.3. (e) For small inter-beam sliding displacements, the total longitudinal stiffness, K_L, is directly related to the shear stiffness, k_s, through Eq. D.8.

To simulate the tip compliance test, a small point force was applied at the tip of the beam assembly (Fig. D1a) and the resulting tip deflection was recorded. The apparent flexural rigidity of the beam was also determined using Eq. 10 of this paper. To simulate the counterbend experiment, a point force was applied to the midpoint of the flagellum (Fig. D1b) to induce a large bend in the proximal section, and the response of distal portion of the beam was examined. To simulate longitudinal shear testing on the isolated axoneme (as in Minoura et al. [1]), we fixed one of the two beams and applied a small concentrated force along the length of the other beam (Fig. D1c). Division of the applied force by the resulting longitudinal displacement of the beam yields a cumulative longitudinal stiffness, K_L, that resists inter-doublet sliding.

Due to the simplicity of our structural model for the axoneme, both the individual spring and longitudinal elastic constants can be expressed in terms of the shear stiffness, k_s. First, consider a unit cell during a small bending deformation accompanied by a small angular displacement, $\Delta\theta \ll 1$ (Fig. D1d), then the extension of the spring is given by

$$\Delta l_k = l - l_0 = \sqrt{(w + h \sin \Delta\theta)^2 + (h \cos \Delta\theta)^2} - \sqrt{w^2 + h^2} \approx \frac{hw\Delta\theta}{\sqrt{w^2 + h^2}}. \qquad (D.1)$$

The perpendicular component of the resulting spring force can be determined and also related to the shear stiffness, k_s , as

$$F_{k_\perp} = k_k \Delta l_k \cos \varphi = k_s \Delta\theta. \qquad (D.2)$$

Using $\cos \varphi = w/\sqrt{w^2 + h^2}$, the spring stiffness can be related to shear stiffness, k_s:

$$k_k = k_s \cdot \frac{h^2 + w^2}{hw^2}. \qquad (D.3)$$

Next, consider a unit cell from the model with one of the two beams having a small relative displacement, ΔL, along the longitudinal direction (Fig. D1e), then the corresponding extension of the spring is given by

$$\Delta l_k = l - l_0 = \sqrt{w^2 + (h + \Delta L)^2} - \sqrt{w^2 + h^2} \approx \frac{h\Delta L}{\sqrt{w^2 + h^2}}. \qquad (D.4)$$

Thus, the longitudinal (along the beam length) component of the resulting spring force can be determined and also related to the longitudinal stiffness as

$$F_{k_\parallel} = k_k \Delta l_k \sin \varphi = k_l \Delta L. \qquad (D.5)$$

Using $\sin \varphi = h/\sqrt{w^2 + h^2}$, we can write:

$$k_l = k_k \cdot \frac{h^2}{h^2 + w^2}. \qquad (D.6)$$

Finally, combining Eqs. 19 and 22, we can express the longitudinal stiffness in terms of the shear stiffness

$$k_l = k_s \cdot \frac{h}{w^2}. \qquad (D.7)$$

Both the spring element stiffness k_k and the resulting longitudinal shear stiffness k_l of each spring element both have units of pN/nm. The cumulative longitudinal stiffness, $K_L = k_l N$, where $N = L/h$ is the number of spring elements (100 in our models). In terms of k_s:

$$K_L = k_s \cdot \frac{L}{w^2} \qquad (D.8)$$

6

We used the simplified 2D finite element computational model above to simulate the tip-bending and counterbend experiments. This model confirms that the apparent flexural rigidity depends on the shear stiffness (Appendix A). When the shear stiffness (as implemented through the elastic constant of the interconnecting springs) is relatively small, there are negligible connections between the two component beams so each individual beam can bend along its own neutral axis. As a result, the apparent flexural rigidity is simply the same as the combined intrinsic flexural rigidity from the two component beams, or $\overline{EI}/EI = 1$ (Fig. D2a). The apparent flexural rigidity increases with increasing shear stiffness until it reaches a plateau for very high spring stiffness (Fig. D2a). The plateau value for the apparent flexural rigidity with very high spring stiffness (higher than the tensile stiffness of the doublets) can be predicted by the parallel axis theorem; the two component beams would extend and compress due to bending along a neutral axis centered between them.

The finite element model also shows that magnitude of the shear stiffness determines the behavior of the distal portion of the flagellum when the proximal region is bent by a concentrated force (Fig. D2b). Small shear stiffness provides little resistance to sliding, and the distal portion of the complex beam remains straight and rotates with the base (Fig. D2b-left panel). For large shear stiffness, there is a sharp, local bend near the point of loading, and the distal portion of the complex beam remains relatively straight (Fig. D2b-right panel). It is only when the shear stiffness is intermediate that the complex beam exhibits a clear counterbend (Fig. D2b-middle panel), like those observed in our experiments.
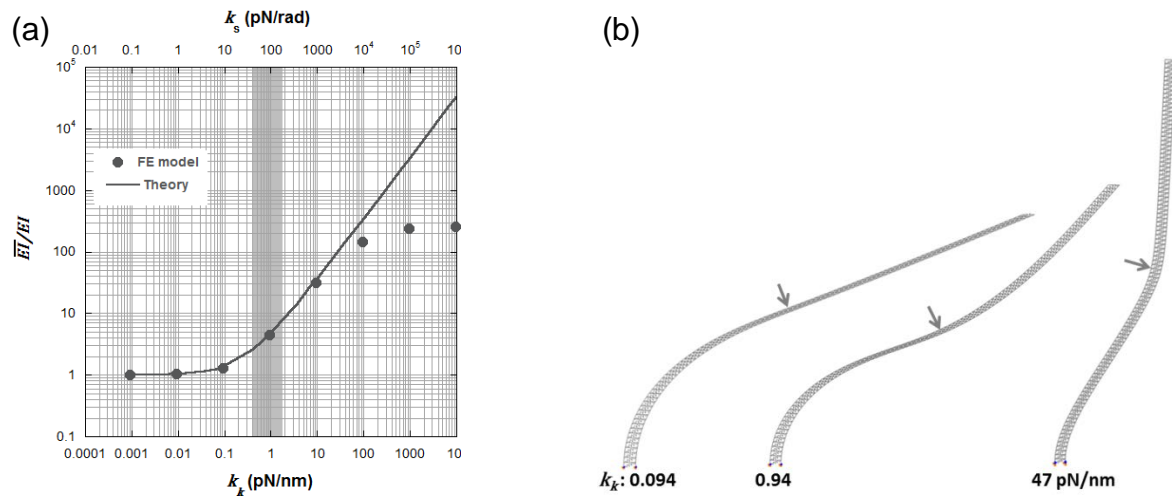
Figure D2. Results from a finite element model of the axoneme show that the tip compliance, apparent flexural rigidity, and counterbend response of the axoneme strongly depend on the inter-doublet shear stiffness, k_s, which depends in turn on the stiffness of connecting springs, k_k (Eq. D.3). (a) The apparent flexural rigidity increases with increasing spring stiffness. When the spring stiffness, k_k, is very small, the apparent flexural rigidity is about the same as the simple sum of the flexural rigidities of the component beams. When the spring stiffness k_k is too large to allow any inter-beam sliding, the apparent flexural rigidity of the whole structure reaches a plateau that can be predicted by the parallel-axis theorem. The shaded region of the data corresponds to the intermediate shear stiffness values estimated from experimental studies of wild-type flagella. Also shown is theoretical curve for the ratio based on Eq. 10 of this paper. (b) When the proximal half of the axoneme model is bent by a concentrated force applied at the mid-point, only the beam with the intermediate shear stiffness (k_k=0.94 pN/nm estimated from the experimental value of k_s=80 pN/rad for wild-type flagella) exhibits a clear counterbend response. From left to right: small, intermediate, and large shear stiffness, respectively.

REFERENCES

[1]   I. Minoura, T. Yagi, and R. Kamiya, "Direct measurement of inter-doublet elasticity in flagellar axonemes," *Cell Struct Funct,* vol. 24, pp. 27-33, Feb 1999.

8